

# Real Space Mapping of Magnetically Quantized Graphene States

David L. Miller,<sup>1</sup> Kevin D. Kubista,<sup>1</sup> Gregory M. Rutter,<sup>2</sup> Ming Ruan,<sup>1</sup> Walt A. de Heer,<sup>1</sup> Markus Kindermann,<sup>1</sup> Phillip N. First,<sup>1,\*</sup> and Joseph A. Stroscio<sup>2,†</sup>

<sup>1</sup>*School of Physics, Georgia Institute of Technology, Atlanta GA, 30332*

<sup>2</sup>*Center for Nanoscale Science and Technology,  
National Institute of Standards and Technology, Gaithersburg MD, 20899*

The symmetry of graphene’s two carbon sublattices underlies its unique electronic structure and half-integer quantum Hall effect. Quantized Hall resistance requires confinement of cyclotron orbits (Landau levels) in the sample interior. Such magnetic localization also may be unique in graphene—especially for  $LL_0$ , the fourfold-degenerate (spin, valley) Landau level straddling graphene’s charge-neutrality energy. Here we map the two-dimensional spatial distribution of  $LL_0$ , using cryogenic scanning tunnelling spectroscopy to measure the local density of states (LDOS) on electronically-decoupled multilayer epitaxial graphene. Unlike disordered LDOS patterns found for conventional 2D electron systems in the quantum Hall regime, above a threshold magnetic field we find an organized pattern of localized states and extended states. In each localized region, an energy gap associated with lattice-scale spatial variation of the LDOS suggests that the sublattice degeneracy (and  $LL_0$  valley degeneracy) is lifted locally. We propose that this occurs when cyclotron orbits become small enough to sample regions of small symmetry-breaking potential originating from a graphene-on-graphene moiré. Our observations, and initial theory, point to rich physics that may come from controlling graphene’s sublattice symmetry.

In 2D electron systems (2DES) the spatial distribution of Landau level (LL) wavefunctions plays a crucial role in the integer quantum Hall effect. Magnetic-field induced localization is essential for the development of well defined Hall conductance plateaus<sup>1</sup> and zero longitudinal

resistance. Transitions between zero-resistance states occur when the Fermi energy coincides with the energy of a spatially-extended “drift state.” Semiclassically, these are cyclotron orbits whose centre drifts along equipotential lines in the sample.<sup>2,3</sup> Graphene has a half-integer quantum Hall effect,<sup>4,5</sup> and the nature of carrier confinement is different than in conventional 2DES due to its gapless energy spectrum and double-valley Fermi surface.<sup>6</sup> These facts alone provide incentive for experimental investigations of the LL spatial distributions in graphene, especially the zero-energy state  $LL_0$ , which lies exactly at the charge neutrality point (Dirac point) and has no semiclassical analog.

But the  $LL_0$  wavefunctions also are unique because of their real-space structure. The  $LL_0$  wavefunction from states in the  $K_+$  valley of the graphene Brillouin zone has wavefunction density on a single sublattice (A) while the wavefunction from the  $K_-$  valley is mirror-identical with density solely on the other (B) sublattice. The wavefunctions are both valley polarized<sup>7-9</sup> and sublattice polarized, an association that is true only for  $LL_0$ . As a consequence of the spin and valley degeneracy of each LL and the position of  $LL_0$  at the Dirac point, magneto-transport measurements<sup>4,5,10</sup> show quantized Hall conductance  $\sigma_{xy} = \nu e^2/h$  for filling factors  $\nu = 4(N \pm 1/2) = \pm 2, \pm 6, \pm 10, \dots$ . Here  $e$  and  $h$  are, respectively, the fundamental unit of charge and Planck’s constant, while  $N = 0, \pm 1, \pm 2, \dots$  labels successive fourfold-degenerate Landau levels (upper/lower signs in these expressions denote states above/below the Dirac point). Recent transport measurements for both monolayer and bilayer graphene reveal apparent interaction effects that lift the energy degeneracy at other integer filling factors,<sup>11-16</sup> and fractional quantum Hall plateaus have recently been observed.<sup>17,18</sup>

With these motivations, here we investigate graphene’s  $LL_0$  as a function of energy, magnetic field, and spatial position in two dimensions. Scanning tunnelling spectroscopy (STS) experiments are performed at 4.3 K in magnetic fields up to 8 T [note that STS differential conductance ( $dI/dV$ ) can be associated with the surface local density of states (LDOS)]. Experimental conditions and sample preparation are identical to earlier work<sup>19</sup> that verified the progression of LL energies,  $E_N \propto \sqrt{|N|B}$ . This is the result expected for the massless charge carriers of *monolayer* graphene and has also been observed in decoupled monolayers on graphite.<sup>20</sup> Here we study the top layer of multilayer epitaxial graphene, where layer-to-layer rotation reduces the coupling between successive graphene sheets, yielding monolayer graphene electrical properties.<sup>21,22</sup> Important experimental details are given under Methods.

Figure 1a shows a scanning tunnelling microscope (STM) topograph of the  $100 \text{ nm} \times 100 \text{ nm}$  area under study. A single defect is visible at the bottom of the image and a hexagonal superlattice height modulation (10 pm root-mean-square variation) is found throughout the region. The superlattice is a consequence of the moiré alignment of two graphene layers rotated slightly with respect to one another. The topographic moiré period of  $(3.98 \pm 0.12) \text{ nm}$  corresponds to a rotation of  $\theta = (3.6 \pm 0.1)^\circ$  between graphene sheets.<sup>23,24</sup> Other than the defect seen in Fig. 1a, the graphene surface is well ordered with the graphene honeycomb lattice apparent in atomically-resolved images, as shown in Fig. 1b.

A perpendicular magnetic field applied to this 2D system creates a spectrum of narrow Landau levels.<sup>19</sup> For magnetic fields of 4 T, 6 T, and 8 T, we acquired  $dI/dV$  spectra at each point on a  $251 \times 251$  grid over the area shown in Fig. 1a. Relevant portions of the  $dI/dV$  data are shown in Fig. 2, and a more complete data set is available as an animation in Supplementary Information. Figure 2a shows grid-averaged spectra of  $\text{LL}_0$  for each magnetic field (we use  $\text{LL}_0^{av}$  to distinguish averaged spectra from single-point spectra). The central  $\text{LL}_0^{av}$  peak grows in intensity and shifts to slightly higher energy with increasing magnetic field due to field-dependent screening of electric fields from the buried SiC/graphene interface and to some extent from the STM tip.<sup>19</sup>  $\text{LL}_0$  is the first LL observed above the Fermi energy  $E_F$  (which lies at zero sample bias), indicating a filling factor  $\nu = -2$  for all three magnetic fields. Small satellite peaks observed in the  $\text{LL}_0$  spectra are discussed in the Supplementary Information (see Supplementary Fig. S5). Circles on the spectra label the energies of the  $dI/dV$  maps displayed in parts b to d (4 T), f to h (6 T), and i to l (8 T) of Fig. 2.

All of the  $dI/dV$  maps show prominent rings around the defect imaged in the topograph of Fig. 1a. These are related to the defect potential and charge state,<sup>25</sup> but a complete analysis is deferred to a later publication. Here we focus on general features of the  $\text{LL}_0$  spatial distribution. The 4 T  $dI/dV$  maps in Figs. 2(b,c,d) display spatial patterns similar to LLs in a conventional 2DES.<sup>26-29</sup> Localized drift states in the tails of the  $\text{LL}^{av}$  follow closed paths around potential energy minima (low energy tail, Fig. 2b) or maxima (high-energy tail, Fig. 2d). The bright triangular ring of large LDOS seen upper-left in Fig. 2b is a good example. The width of the closed path is approximately the magnetic length ( $\ell_B = \sqrt{\hbar/(2\pi eB)}$ ), which is the size of the  $\text{LL}_0$  wavefunction (see  $\ell_B$  bars in right column). Bright and dark regions in Fig. 2d and Fig. 2b are complementary, consistent with the localization picture presented. At the central energy,

Fig. 2c shows that the extent of the drift state expands drastically. In the integer quantum Hall effect, coupling of edge states through this extended state destroys the zero longitudinal magnetoresistance.

The wavefunction size  $\ell_B$  determines how accurately drift states can follow the local potential landscape, as shown schematically in Fig. 2e. The same features found at 4 T are seen more clearly resolved in the  $dI/dV$  maps at 6 T [Figs. 2(f,g,h)] and 8 T [Figs. 2(i,j,k,l)] (*cf.*, the ring at upper-left in b,f,i,j). New features also appear: The extended state in Figs. 2g and 2k develops a pattern with high density of states confined to narrow channels separating lower-density patches of diameter  $> \ell_B$ . These patches form a distorted hexagonal array and show large pixel-to-pixel fluctuation of intensity (the fluctuations are most apparent in Figs. 2f and 2j; see also the data animation file included in Supplementary Information). Magnetically induced LDOS variation on a length scale  $\ll \ell_B$  is unexpected and qualitatively different from any previous measurements on a conventional 2DES.

In Fig. 3a we track the energy of the  $LL_0$  peak as a function of position [ $E_0(x, y)$ ; see Supplementary Information] for the 8 T map data. A region of high peak-energy is apparent near the topographic defect (see Fig. 1a). A second broad maximum can be seen in the upper-right quadrant of Fig. 3a, while a dip in  $E_0(x, y)$  occurs near the top-centre. Within the drift state picture,  $LL_0$  follows equipotential lines for length scales greater than  $\ell_B$ , therefore we associate these broad  $E_0(x, y)$  features with hills and valleys in the electron potential energy landscape. The increase in  $E_0$  over the topographic defect (bottom-centre) is consistent with a negatively-charged configuration. The sources of the second potential energy maximum (upper-right) and the potential energy minimum (top-centre) are not resolved in the topograph, but a natural explanation would be the presence of other isolated defects or intercalant atoms.

Inside each of the patches identified above, the peak-tracking map shows a speckled pattern, indicating large pixel-to-pixel variation of  $E_0$ . An expanded view of the speckle within box I of part (a) is shown in Fig. 3b. From this patch and from a region that shows no speckle (box II), we produce histograms of  $E_0$  values, as shown in Fig. 3c. In region II, all  $LL_0$  peaks are found to lie close to the mean energy. Within patch I, however,  $E_0$  values cluster around two distinct energies separated by more than 6 meV.

These observations firmly establish that the LDOS energy distribution varies on the atomic scale within each speckled patch. Clearly, this behaviour falls outside of the drift state picture

and—unlike the broad maxima and minima in  $E_0(x, y)$ —does not appear to be associated with isolated defects. At 0.4 nm pixel spacing, the atomic lattice (0.246 nm lattice constant, 0.142 nm C-C bond length) is under-sampled in these LDOS maps due to time constraints in data acquisition, but the *resolution* is  $\ll 0.4$  nm (*cf.* Fig. 1b, acquired with the same STM tip), i.e., a large sampling increment does not broaden underlying features. Therefore, the exact atomic LDOS is not determined directly in the present data, but the bimodal distribution of  $LL_0$  peak energies clearly suggests different LDOS on the A and B carbon sublattices. Given the association of valley and sublattice in  $LL_0$ , the histogram energy gap is “valley-splitting.”

Figure 3d shows the average spectrum from the high-count bin at the center of the low-energy peak of the histogram (labelled A; see Supplementary Information) and the average spectrum from the high-count bin in the high-energy peak (B). With the caveat above, we interpret these as the LDOS spectra from A and B sublattices.

The spatial and magnetic field variation of valley-splitting in the  $LL_0$  states can be seen in profiles of the  $dI/dV$  intensity versus energy along a line crossing one of the speckled patches. Figures 4(a,b,c) show these spectral profiles taken from  $dI/dV$  maps at magnetic fields of, respectively, 4 T, 6 T, and 8 T. In the 4 T profile, the peak energy  $E_0$  dips slightly over the patch, but does not split. At 6 T a clear energy gap develops, reaching a maximum of  $\approx 8$  meV, but no gap is found in unspeckled regions. By 8 T the splitting has increased slightly to  $\approx 10$  meV. Hence the valley-splitting occurs only above a threshold field  $B_*$  where  $4 \text{ T} < B_* < 6 \text{ T}$  and may saturate at high fields to a value somewhat larger than 10 meV. (Close examination of Figs. 4b and 4c also shows anticorrelation of the  $dI/dV$  intensity in the two bands, as expected from the pixel-to-pixel fluctuations seen in the 2D  $dI/dV$  maps of Fig. 2—see also Supplementary Figs. S1 and S2.)

Any explanation of this newly-discovered valley-splitting must also address the large scale spatial distribution of the valley-split patches. The characteristics of this pattern are summarized in the “gap map”<sup>30</sup> of Fig. 5a. In this 8 T map, colour corresponds to the local energy gap  $\Delta = E_0(B) - E_0(A)$ , where  $E_0(A)$  and  $E_0(B)$  are the energies of the respective histogram peaks (e.g., Fig. 3c). As indicated in 5a, the valley-split patches form a large hexagon (slightly distorted), with sides of length  $\approx 40$  nm. In Fig. S3, we show that partial patches at the edges of the gap map are consistent with a repeating pattern of patches with a 70 nm period. Gap maps for magnetic fields of 6 T and 4 T can be found in Fig. S4, which shows that the

long-range pattern is nearly identical at 8 T and 6 T (with similar maximum energy gaps), but at 4 T the valley-split patches vanish entirely, as seen also in Fig. 4a.

Before delving into theoretical possibilities, we summarize our new experimental discoveries:

- 1) We have imaged the  $LL_0$  drift states of graphene, identifying magnetically-localized states above and below the Dirac point, and an extended state that lies at the peak energy of  $LL_0^{av}$ . The drift states follow equipotentials over length scales larger than the magnetic length  $\ell_B$ .
- 2) Above a threshold magnetic field  $B_* \gtrsim 4$  T, we find spatial variation of the  $LL_0$  energy on the atomic scale. These variations occur only within small patches of size comparable to the magnetic length. Within each patch, two distinct spectra are found, with the difference in  $LL_0$  energies apparently saturating to  $\approx 10$  meV for fields greater than  $B_*$ . The two spectra appear to be due to different local density of states on the  $A$  and  $B$  carbon sublattices. The valley-split patches themselves form a larger hexagonal pattern that appears to repeat with a period of  $\approx 70$  nm.

The presence of magnetically-localized states and the extended state are essential for the observation of the half-integer quantum Hall effect in graphene. From our results it appears that the basics of the drift-state picture remain valid at energies both above and below  $LL_0^{av}$ . However, atomic-scale spatial variation of  $LL_0$  with the accompanying large-area pattern of valley-split patches is both unexpected and unpredicted. In what follows, we discuss potential explanations of this valley-splitting.

Pauli exclusion and Coulomb correlations in a many-electron system typically lift the degeneracies of independent-electron states. For graphene, the theory of correlated states continues to evolve,<sup>6</sup> and in most cases no spatial inhomogeneity is predicted. A few models, such as a ground state Wigner crystal/bubble phase<sup>31</sup> or a pseudospin vortex lattice,<sup>32</sup> could produce spatial inhomogeneity comparable to the pattern that we observe. We do not exclude a many-body state as the source our findings, but there are at least three issues that may discount any such explanation: 1) The Fermi energy lies 44 meV to 56 meV below the  $LL_0^{av}$  density-of-states peak (Fig. 2a). Creation of an energy gap in the unfilled states of  $LL_0$  would not lower the total energy of the system. 2) The spatial distribution of valley-split patches does not vary with magnetic field from 6 T to 8 T. In the absence of pinning centres, a pattern created by density-dependent interactions should change with magnetic field since the  $LL$  density of states varies with field. 3) A high density electron-doped layer ( $n \approx 5 \times 10^{12} \text{ cm}^{-2}$ ) lies at the interface

with the silicon carbide substrate, less than 4 nm below the top graphene layer in the multilayer stack.<sup>21,22</sup> Screening by this interface layer should reduce Coulomb correlations. This doesn't preclude an interaction-driven state, but formation of a pattern with a unit cell much larger than the film thickness would be less probable.

In light of these issues, we look for an explanation within the independent-electron picture. A small contribution of intervalley orbital currents is known to lift the  $LL_0$  valley degeneracy,<sup>33</sup> but the predicted energy gap is even smaller than the ordinary Zeeman splitting (i.e.,  $\lesssim \mu_B B$ , where  $\mu_B$  is the Bohr magneton), which itself is unobserved in these four-Kelvin experiments. We propose instead that our observations indicate a subtle interaction of graphene with the layers below, which comprise an atomically-smooth and ordered substrate.

Considering any two layers in multilayer epitaxial graphene (not necessarily adjacent layers) rotated by a small angle, there are alternating regions of high atomic alignment between the layers. These regions fall into two categories: 1) locally sublattice-equivalent alignment where every top-layer atom lies directly above an atom in the lower layer. We refer to these regions as AA. 2) locally sublattice-inequivalent alignment where A atoms from the top layer lie over B atoms in the lower layer or vice-versa. These areas we refer to as AB/BA. A model moiré superlattice is shown in Fig. 5b. Regions of AA, AB, and BA stacking are apparent within the superlattice cell, such that the sublattices remain equivalent over the full supercell and the linear band dispersion of graphene is preserved near the Dirac point<sup>24,34-38</sup> (superlattice van Hove singularities<sup>39</sup> were not found within the energy range of our  $dI/dV$  maps). Figure 5c illustrates how multiple layers typically have different rotational alignment. STM topographs over other regions of this sample show the effect of one moiré interfering with another below it (a double moiré), easily creating superlattice periods of tens of nanometres<sup>19</sup> and requiring the participation of at least 3 graphene layers, as illustrated.

AB/BA stacking creates different environments for atoms on different sublattices, which can be modelled phenomenologically as a small difference in on-site potential (the “staggered potential”). For magnetic fields where  $\ell_B$  is much larger than the size of the AB/BA patches, the staggered potential has little effect, but at fields where the wavefunction size becomes smaller than an AB/BA patch, the staggered potential is important. Figures 5d and 5e illustrate the  $LL_0$  LDOS distribution over the A/B sublattices and the effect on the energy spectrum induced by the staggered potential. This simple picture explains the appearance above a threshold field

of a hexagonal array of valley-split patches over the AB/BA regions. As shown in Fig. 5b, straining one graphene lattice uniaxially by less than 0.25% with respect to the other accounts for the distortion of the superlattice cell from a regular hexagon.<sup>40</sup> Considering a perturbative approach, the sublattice-polarized LDOS distribution of  $LL_0$  is also explained since wavefunctions are unaffected in the first-order of perturbation (in fact, to all orders for a uniform staggered potential). However, the observed valley-splitting is smaller than one might naively anticipate from an interaction between first (top) and second graphene layers. More importantly, the size of the presumed moiré pattern is much larger than the single moiré superlattice imaged in the topography (which we attribute to the first and second graphene layers). Therefore, although in Fig. 1 we do not directly image the moiré between first and *third* graphene layers, we suggest that this is the interaction responsible for the spatially inhomogeneous valley splitting.

The proposed mechanism has some similarities to a lattice-scale charge density wave.<sup>41–43</sup> It is conceivable that the interlayer interaction could locally promote this type of instability, but in the present case, no energy would be gained by opening a gap in the unoccupied  $LL_0$ . In Supplementary Information, we develop a phenomenological model to investigate the influence of a small staggered potential and spatial inhomogeneity in the staggered potential arising from the moiré alignment of graphene layers. Consideration of the microscopic foundations of the model (using tight-binding parameters fitted to experiment)<sup>44,45</sup> shows that our observed valley splitting of  $\approx 10$  meV is consistent with a first-layer/third-layer interaction. The model also produces a sublattice-polarized LDOS and an exponential suppression of the valley-splitting for moiré period  $\ell \lesssim \ell_B$ . The latter result implies a threshold magnetic field  $B_*$  determined by  $\ell_B \approx \ell$ , which furthermore explains the negligible influence of the 4 nm first-layer/second-layer moiré on the valley splitting since  $\ell_B \gg 4$  nm at all fields studied here.

Our experimental evidence for local lifting of the valley degeneracy in graphene’s zero-Landau level has important implications for transport phenomena. Spatial modulation of the sublattice symmetry may account for prior observations of fractal-like structure in magnetoresistance measurements of this material.<sup>46</sup> The underlying physics discovered here should apply to other atomically-flat substrates or overlayers—such as twisted bilayer graphene or graphene on boron nitride—and suggests that strain and accidental layer slip (e.g., at contacts) may be important to consider in measurements of nominally graphite-stacked graphene bilayers. The alternating pattern of AB- and BA-aligned regions in the moiré also implies that bands of the

same energy have opposite sublattice symmetry in neighbouring valley-split patches. With gate control of the carrier density, one could position the Fermi energy between the valley-split levels to create a pattern of orthogonal Fermi fluids having graphene-like superlattice symmetry. The physics of both single-layer and interlayer correlations and coherence in such a system would be interesting.

## Methods

Graphene was prepared by epitaxial growth via thermal decomposition of a hydrogen-etched 4H-SiC(000 $\bar{1}$ ) surface in a low vacuum induction furnace.<sup>21,46,47</sup> The sample was then outgassed at 1250 °C for 5 min in ultrahigh vacuum (UHV) to remove adsorbates. During growth, multiple graphene layers form and stack in a non-graphitic sequence of rotated layers. Rotational stacking results in moiré alignments of layers that largely decouples their electronic properties. The moiré is often visible in STM topographs as a small hexagonal superlattice modulation in the apparent surface height (10 pm RMS in the area studied). As measured by ellipsometry, the sample thickness was  $10 \pm 1$  layers. The sample was studied in UHV at a temperature of 4.3 K using a custom-built cryogenic STM at NIST. The Ir tip was prepared *ex situ* using electrochemical etching, and then heated *in situ* by electron bombardment and further cleaned by field evaporation during imaging via field ion microscopy.

Spectra of the local differential conductance ( $dI/dV$ ) are collected by fixing the tip-sample distance and sweeping the bias voltage. Using a lock-in amplifier to modulate the sample bias ( $f_{mod} = 500$  Hz,  $V_{mod} = 2$  mV), the resulting signal ( $dI/dV$  vs.  $V$ ) is collected. Spectra were collected in a  $251 \times 251$  grid over a  $100 \text{ nm} \times 100 \text{ nm}$  area at  $(x, y)$  sample increments of 0.4 nm and for magnetic fields of 4 T, 6 T and 8 T.  $dI/dV$  map acquisition times were  $\approx 65$  h (100-point spectra) at each magnetic field. The topography was recorded simultaneously at 0.1 nm increments with a sample bias of  $V_s = 0.35$  V and a tunnelling current of  $I_s = 400$  pA.

## Acknowledgments

We thank C. Berger, M. Sprinkle, N. Sharma, S. Blankenship, A. Band, and F. Hess for their technical contributions to this work. Funding from NSF (DMR-0804908), the Semiconductor Research Corporation Nanoelectronics Research Initiative (NRI-INDEX), and the W. M. Keck Foundation are

gratefully acknowledged. Graphene production facilities of the Georgia Tech MRSEC (NSF DMR-0820382) were employed.

---

\* Electronic address: `first@gatech.edu`

† Electronic address: `joseph.stroscio@nist.gov`

- <sup>1</sup> Davies, J. H. *The physics of low-dimensional semiconductors : An introduction* (Cambridge University Press, Cambridge, UK, 1998).
- <sup>2</sup> Ando, T. Electron localization in a two-dimensional system in strong magnetic fields. II: Long-range scatterers and response functions. *J. Phys. Soc. Jpn.* **53**, 3101–3111 (1984).
- <sup>3</sup> Huckestein, B. Scaling theory of the integer quantum Hall effect. *Rev. Mod. Phys.* **67**, 357–396 (1995).
- <sup>4</sup> Zhang, Y., Tan, Y.-W., Stormer, H. L. & Kim, P. Experimental observation of the quantum Hall effect and Berry’s phase in graphene. *Nature* **438**, 201–204 (2005).
- <sup>5</sup> Novoselov, K. S. *et al.* Two-dimensional gas of massless Dirac fermions in graphene. *Nature* **438**, 197–200 (2005).
- <sup>6</sup> Castro Neto, A. H., Guinea, F., Peres, N. M. R., Novoselov, K. S. & Geim, A. K. The electronic properties of graphene. *Rev. Mod. Phys.* **81**, 109 (2009). For a recent review.
- <sup>7</sup> Pereira, A. L. C. & Schulz, P. A. Valley polarization effects on localization in graphene Landau levels. *Phys. Rev. B* **77**, 075416 (2008).
- <sup>8</sup> Beenakker, C. W. J. Colloquium: Andreev reflection and Klein tunneling in graphene. *Rev. Mod. Phys.* **80**, 1337 (2008).
- <sup>9</sup> Pereira, A. L. C. Splitting of critical energies in the  $n=0$  Landau level of graphene. *New J. Phys.* **11**, 095019 (13pp) (2009).
- <sup>10</sup> Wu, X. *et al.* Half integer quantum Hall effect in high mobility single layer epitaxial graphene. *Appl. Phys. Lett.* **95**, 223108 (2009).
- <sup>11</sup> Checkelsky, J. G., Li, L. & Ong, N. P. Divergent resistance at the Dirac point in graphene: Evidence for a transition in a high magnetic field. *Phys. Rev. B* **79**, 115434 (2009).
- <sup>12</sup> Checkelsky, J. G., Li, L. & Ong, N. P. Zero-energy state in graphene in a high magnetic field. *Phys. Rev. Lett.* **100**, 206801 (2008).

- <sup>13</sup> Jiang, Z., Zhang, Y., Stormer, H. L. & Kim, P. Quantum Hall states near the charge-neutral Dirac point in graphene. *Phys. Rev. Lett.* **99**, 106802 (2007).
- <sup>14</sup> Zhang, Y. *et al.* Landau-level splitting in graphene in high magnetic fields. *Phys. Rev. Lett.* **96**, 136806 (2006).
- <sup>15</sup> Feldman, B. E., Martin, J. & Yacoby, A. Broken-symmetry states and divergent resistance in suspended bilayer graphene. *Nature Phys.* **5**, 889–893 (2009).
- <sup>16</sup> Zhao, Y., Cadden-Zimansky, P., Jiang, Z. & Kim, P. Symmetry breaking in the zero-energy Landau level in bilayer graphene. *Phys. Rev. Lett.* **104**, 066801 (2010).
- <sup>17</sup> Du, X., Skachko, I., Duerr, F., Luican, A. & Andrei, E. Y. Fractional quantum Hall effect and insulating phase of Dirac electrons in graphene. *Nature* **462**, 192–195 (2009).
- <sup>18</sup> Bolotin, K. I., Ghahari, F., Shulman, M. D., Stormer, H. L. & Kim, P. Observation of the fractional quantum Hall effect in graphene. *Nature* **462**, 196–199 (2009).
- <sup>19</sup> Miller, D. L. *et al.* Observing the quantization of zero mass carriers in graphene. *Science* **324**, 924–927 (2009).
- <sup>20</sup> Li, G., Luican, A. & Andrei, E. Y. Scanning tunneling spectroscopy of graphene on graphite. *Phys. Rev. Lett.* **102**, 176804 (2009).
- <sup>21</sup> de Heer, W. A. *et al.* Epitaxial graphene. *Solid State Commun.* **143**, 92–100 (2007).
- <sup>22</sup> First, P. N. *et al.* Epitaxial graphenes on silicon carbide. *MRS Bulletin* **35**, 296–305 (2010).
- <sup>23</sup> All uncertainties reported represent one standard deviation in the measured quantity. Error is calculated from the position of the intensity spots of the FT.
- <sup>24</sup> Hass, J. *et al.* Why multilayer graphene on 4H-SiC(000 $\bar{1}$ ) behaves like a single sheet of graphene. *Phys. Rev. Lett.* **100**, 125504 (2008).
- <sup>25</sup> Martin, J. *et al.* The nature of localization in graphene under quantum hall conditions. *Nature Phys.* **5**, 669–674 (2009).
- <sup>26</sup> Morgenstern, M., Klijn, J., Meyer, C., Haude, D. & Wiesendanger, R. Visualizing the influence of interactions on the nanoscale: Simple electron systems. In Koenraad, P. M. & Kemerink, M. (eds.) *Scanning Tunneling Microscopy/Spectroscopy and Related Techniques: 12th International Conference*, vol. 696 of *AIP Conference Proceedings*, 11–19 (AIP, Melville, NY, 2003). URL <http://link.aip.org/link/?APC/696/11/1>.
- <sup>27</sup> Morgenstern, M., Klijn, J., Meyer, C. & Wiesendanger, R. Real-space observation of drift states

- in a two-dimensional electron system at high magnetic fields. *Phys. Rev. Lett.* **90**, 056804 (2003).
- <sup>28</sup> Hashimoto, K. *et al.* Quantum Hall transition in real space: From localized to extended states. *Phys. Rev. Lett.* **101**, 256802 (2008).
- <sup>29</sup> Niimi, Y., Kambara, H. & Fukuyama, H. Localized distributions of quasi-two-dimensional electronic states near defects artificially created at graphite surfaces in magnetic fields. *Phys. Rev. Lett.* **102**, 026803 (2009).
- <sup>30</sup> Pan, S. H. *et al.* Microscopic electronic inhomogeneity in the high- $T_c$  superconductor  $\text{Bi}_2\text{Sr}_2\text{CaCu}_2\text{O}_{8+x}$ . *Nature* **413**, 282–285 (2001).
- <sup>31</sup> Poplavskyy, O., Goerbig, M. O. & Smith, C. M. Local density of states of electron-crystal phases in graphene in the quantum Hall regime. *Phys. Rev. B* **80**, 195414 (2009).
- <sup>32</sup> Nomura, K., Ryu, S. & Lee, D.-H. Field-induced Kosterlitz-Thouless transition in the  $n = 0$  Landau level of graphene. *Phys. Rev. Lett.* **103**, 216801 (2009).
- <sup>33</sup> Luk'yanchuk, I. A. & Bratkovsky, A. M. Lattice-induced double-valley degeneracy lifting in graphene by a magnetic field. *Phys. Rev. Lett.* **100**, 176404 (2008).
- <sup>34</sup> Hass, J., de Heer, W. A. & Conrad, E. H. The growth and morphology of epitaxial multilayer graphene. *J. Phys.: Condens. Matter* **20**, 323202 (2008).
- <sup>35</sup> Sprinkle, M. *et al.* First direct observation of a nearly ideal graphene band structure. *Phys. Rev. Lett.* **103**, 226803 (2009).
- <sup>36</sup> Latil, S., Meunier, V. & Henrard, L. Massless fermions in multilayer graphitic systems with misoriented layers: Ab initio calculations and experimental fingerprints. *Phys. Rev. B* **76**, 201402 (2007).
- <sup>37</sup> Lopes dos Santos, J. M. B., Peres, N. M. R. & Castro Neto, A. H. Graphene bilayer with a twist: Electronic structure. *Phys. Rev. Lett.* **99**, 256802–4 (2007).
- <sup>38</sup> Mele, E. J. Commensuration and interlayer coherence in twisted bilayer graphene. *Phys. Rev. B* **81**, 161405(R) (2010).
- <sup>39</sup> Li, G. *et al.* Observation of van Hove singularities in twisted graphene layers. *Nature Phys.* **6**, 109–113 (2010).
- <sup>40</sup> Miller, D. L. *et al.* Structural analysis of multilayer graphene via atomic moiré interferometry. *Phys. Rev. B* **81**, 125427 (2010).
- <sup>41</sup> Fuchs, J.-N. & Lederer, P. Spontaneous parity breaking of graphene in the quantum Hall regime.

- Phys. Rev. Lett.* **98**, 016803 (2007).
- <sup>42</sup> Alicea, J. & Fisher, M. P. A. Graphene integer quantum Hall effect in the ferromagnetic and paramagnetic regimes. *Phys. Rev. B* **74**, 075422 (2006).
- <sup>43</sup> Khveshchenko, D. V. Magnetic-field-induced insulating behavior in highly oriented pyrolytic graphite. *Phys. Rev. Lett.* **87**, 206401– (2001).
- <sup>44</sup> Partoens, B. & Peeters, F. M. From graphene to graphite: Electronic structure around the K point. *Phys. Rev. B* **74**, 075404 (2006).
- <sup>45</sup> Dresselhaus, M. S. & Dresselhaus, G. Intercalation compounds of graphite. *Adv. Phys.* **51**, 1–186 (2002).
- <sup>46</sup> Berger, C. *et al.* Electronic confinement and coherence in patterned epitaxial graphene. *Science* **312**, 1191–1196 (2006).
- <sup>47</sup> Berger, C. *et al.* Ultrathin epitaxial graphite: 2D electron gas properties and a route toward graphene-based nanoelectronics. *J. Phys. Chem. B* **108**, 19912–19916 (2004).

## I. AUTHOR CONTRIBUTIONS

D.L.M., K.D.K., G.M.R., P.N.F., and J.A.S. performed the measurements in the 4K UHV STM facility in the CNST at NIST. The graphene sample was grown by M.R. and W.A. dH at Georgia Tech. A theoretical analysis of the epitaxial graphene multilayer system was performed by M.K.

## II. AUTHOR INFORMATION

The authors declare no competing financial interests. Correspondence and requests for materials should be addressed to P.N.F (first@gatech.edu) and J.A.S. (joseph.stroscio@nist.gov).

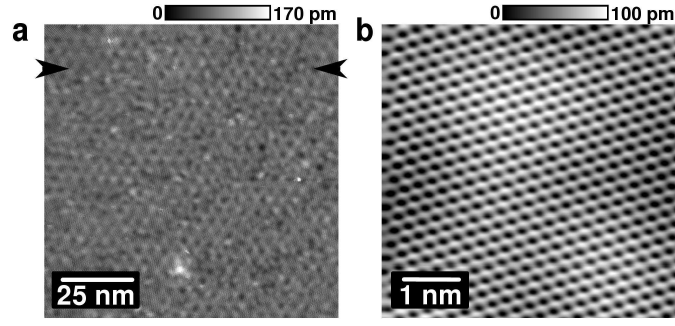


FIG. 1: Topographic STM images of the multilayer epitaxial graphene sample grown on SiC. (a) A  $100 \text{ nm} \times 100 \text{ nm}$  real-space image of the surface studied, taken at a sample bias of  $V_s = 0.35 \text{ V}$  and a tunnel current  $I_s = 400 \text{ pA}$ . This image was acquired simultaneously with the 8 T  $dI/dV$  maps shown in Fig. 2. Periodic height variations are a moiré pattern of  $\approx 4 \text{ nm}$  period. A defect at bottom-centre distorts the topograph due to an electronic perturbation. Arrows label the line corresponding to the spectral profiles of Fig. 4. (b) A  $5 \text{ nm} \times 5 \text{ nm}$  image ( $V_s = 0.10 \text{ V}$ ,  $I_s = 100 \text{ pA}$ ,  $x, y$  sampling increment  $25 \text{ pm}$ ) showing the atomic lattice.

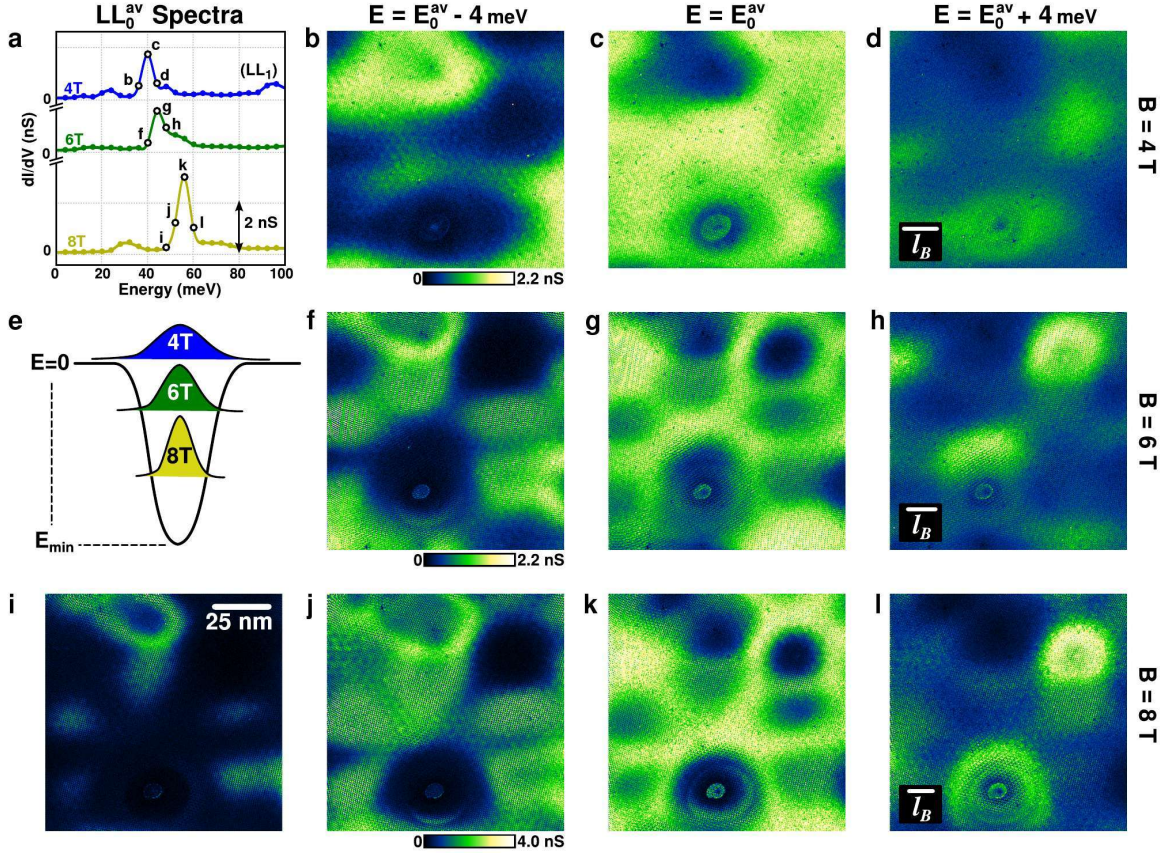


FIG. 2: STS  $dI/dV$  maps showing an extended state at the  $LL_0^{av}$  peak energy ( $E_0^{av}$ ) and localized states at energies above and below  $E_0^{av}$ . (a) Spectra of  $LL_0^{av}$  at magnetic fields of 4 T, 6 T and 8 T averaged over the area in Fig. 1a. Energy (throughout the paper) is  $eV_s$ , where  $V_s$  is the sample voltage bias. Labels at marked energies (open circles) correspond to the displayed maps. Lines are spline interpolants of the raw data (filled circles). STS  $dI/dV$  maps of the  $100 \text{ nm} \times 100 \text{ nm}$  region are displayed for magnetic fields of 4 T (b–d), 6 T (f–h), and 8 T (i–l). These maps taken from a larger data set were selected at energies bracketing  $E_0^{av}$  for each magnetic field (note that areas probed at different fields are not in exact registry; the defect position can be used as an alignment guide). The magnetic lengths ( $\ell_B$ ) shown in d, h, l correspond to values of 13 nm, 10.5 nm and 9 nm, respectively. (e) Schematic of the  $LL_0$  wavefunction shrinking under increasing magnetic field. Smaller drift-state wavefunctions track equipotentials deeper within an extremum in the potential-energy landscape. Following the maps down columns (e.g., c, g, k at the  $LL_0^{av}$  peak energy  $E_0^{av}$ ) shows that  $dI/dV$  features sharpen due to decreasing  $\ell_B$ . Left to right across rows, the maps show the change from states localized in potential energy minima, to extended states at  $E_0^{av}$ , to states localized around potential energy maxima (note the inversion of  $dI/dV$  intensity from  $E_0^{av} - 4 \text{ meV}$  to  $E_0^{av} + 4 \text{ meV}$ ). Rings at upper-left in (i) and (j) can be viewed as tracing equipotential lines that differ by 4 mV. At energy  $E_0^{av}$ , the drift state follows an equipotential that may span the sample. In 6 T and 8 T maps, patches with large pixel-to-pixel intensity variation appear.

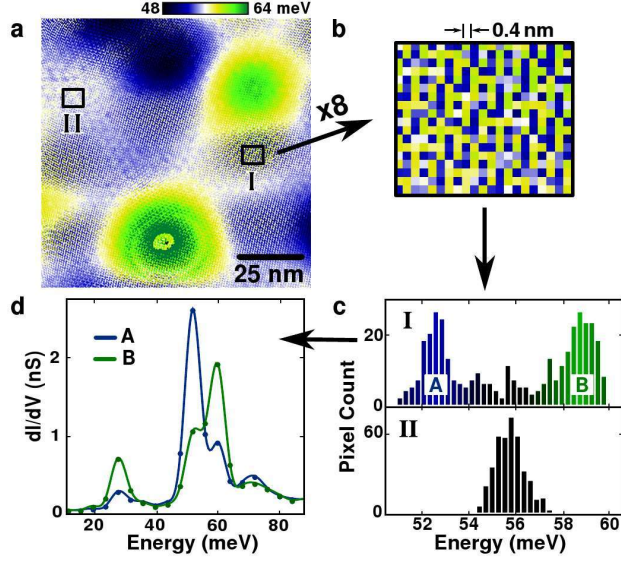


FIG. 3: Spatial variation of the  $LL_0$  energy and the local lifting of valley degeneracy. (a) Spatial map of the  $LL_0$  peak energy  $E_0(x, y)$  (colour scale) derived from 8 T  $dI/dV$  map data. Over much of the area,  $E_0$  varies smoothly, reaching a maximum at the position of the defect seen in Fig. 1a (omitting the defect core). A second maximum (top-right) and a minimum (top-centre) could be due to unresolved defects. Several speckled patches can be seen, where  $E_0$  varies over distances shorter than the 0.4 nm sampling distance. (b) Expanded view of the speckle displaying large pixel-to-pixel variations of  $E_0$ . (c) Histograms of  $E_0$  values from boxes I & II in part (a). In the speckled patch I, the histogram (top) has two distinct peaks (A & B) separated by 6 meV. A single peak is found in the bottom histogram from unspeckled region II. (d) Average  $dI/dV$  spectrum obtained from pixels in the high-count bin ( $52.5 \text{ meV} < E_0 < 52.75 \text{ meV}$ ) under histogram peak A (blue) and from pixels in the high-count bin ( $58.5 \text{ meV} < E_0 < 58.75 \text{ meV}$ ) under peak B (green). We associate these with the valley-split  $LL_0$  LDOS on sublattices A and B.

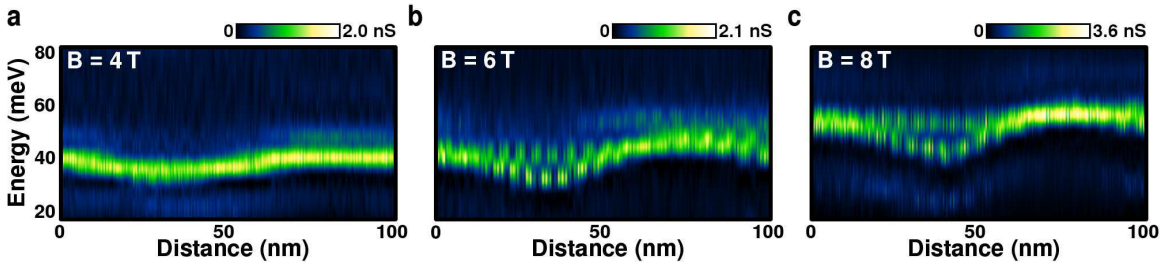


FIG. 4: Magnetic field dependence of the spatially varying  $LL_0$  peak energy. Panels show the  $dI/dV$  magnitude (colour) versus energy (vertical) and position (horizontal) along the line marked by arrows in Fig. 1a. The spectral profiles were extracted from  $dI/dV$  maps at (a) 4 T, (b) 6 T, and (c) 8 T. The bright  $dI/dV$  peak is  $LL_0$ . Within a speckled patch centred at 35–40 nm, an energy gap is observed for fields above 4 T. The  $dI/dV$  intensity of the two bands is anticorrelated: At any spatial position (pixel), large  $dI/dV$  in one band corresponds to small  $dI/dV$  in the other. Note that the  $\approx 5 \text{ nm}$  intensity modulation of the bands is an aliasing artifact due to undersampling of the graphene lattice.

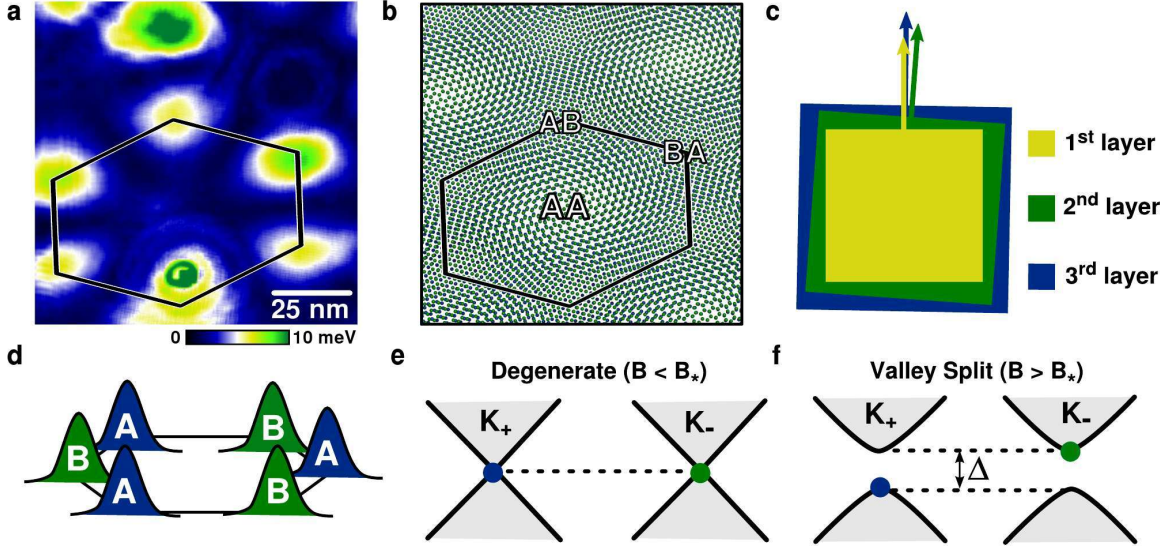


FIG. 5: Energy-gap map and proposed model of the local valley splitting. (a) A gap map derived from the 8 T  $dI/dV$  data, displaying the size of the  $LL_0$  valley-split energy gap,  $\Delta = E_0(B) - E_0(A)$ , as a function of spatial position (Supplementary Fig. S4 shows gap maps at 4 T and 6 T).  $\Delta$  is determined over a (moving) box of size  $1.2 \text{ nm} \times 1.2 \text{ nm}$  (9 pixels). (b) Model of the moiré alignment of two graphene sheets. The top model layer (green) is aligned with the sample crystallographic axes, but the atomic unit cell is larger for illustration. The second model layer (blue) is slightly rotated with respect to the top layer and strained uniaxially by 0.25%. The model shows that the observed quasi-hexagonal symmetry in (a) follows naturally from a large moiré superlattice with small relative strain.<sup>40</sup> The valley-split patches in (a) correspond to AB/BA patches in the model. Since this large moiré superlattice is not seen in the topography, the energy gaps are most likely a consequence of interaction between the first (top) and third graphene layers. (c) Schematic of an orientation of the top three layers that would produce the observed short-period (STM) and long-period (STS) moiré patterns. (d) Schematic wavefunctions of  $LL_0$  in graphene. A and B label the sublattice atoms; blue denotes states from the  $K_+$  valley of the graphene Brillouin zone and green corresponds to states from the  $K_-$  valley. (e) Schematic of  $LL_0$  states at the  $K_{\pm}$  points with zero potential difference between sublattices (zero staggered potential). (f)  $LL_0$  states at the  $K_{\pm}$  points with nonzero staggered potential.

# Supplementary Information – Real Space Mapping of Magnetically Quantized Graphene States

David L. Miller,<sup>1</sup> Kevin D. Kubista,<sup>1</sup> Gregory M. Rutter,<sup>2</sup> Ming Ruan,<sup>1</sup> Walt A. de Heer,<sup>1</sup> Markus Kindermann,<sup>1</sup> Phillip N. First,<sup>1,\*</sup> and Joseph A. Stroscio<sup>2,†</sup>

<sup>1</sup>*School of Physics, Georgia Institute of Technology, Atlanta GA, 30332*

<sup>2</sup>*Center for Nanoscale Science and Technology, National Institute of Standards and Technology, Gaithersburg MD, 20899*

## I. DATA ANALYSIS

*E<sub>0</sub>(x, y) Maps:* For Fig. 3a, the energy of the LL<sub>0</sub>  $dI/dV$  maximum ( $E_0$ ) was determined by fitting a Lorentzian peak to the spectrum at each  $(x, y)$  pixel, using a nonlinear least squares algorithm (Levenberg-Marquardt in MINPACK). Fit parameters were the peak-center energy  $E_0$ , the Lorentzian width, and the peak amplitude. Figure 3a plots the fitted  $E_0$  values at each pixel.

*A/B Spectra:* The blue spectrum (“A”) in Fig. 3d is the average of those spectra from region I whose  $E_0$  value lies in the high-count bin of the “A” peak of the bimodal (upper) histogram in Fig. 3c. From the figure, this includes 25 spectra with  $52.5 \text{ meV} < E_0 < 52.75 \text{ meV}$ . The green spectrum (“B”) in Fig. 3d is the average of those spectra from region I whose  $E_0$  lies in the high-count bin of the “B” peak of the histogram in Fig. 3c. From the figure, this includes 25 spectra with  $58.5 \text{ meV} < E_0 < 58.75 \text{ meV}$ . In Fig. 3d, the LL<sub>0</sub> peaks appear to be separated by a slightly larger energy than the 6 meV separation of the histogram maxima. This is because for the histogram, we use Lorentzian peak-fitting over a small energy range to extract an accurate  $E_0$  at each spatial pixel, but for the average spectra we simply average the raw (uninterpolated) data points. The blue and green lines in Fig. 3d are spline fits to the average spectra given as guides to the eye. The detailed spectral shape is ultimately limited by our energy sampling, but the fact that there are two distinct spectra with different  $E_0$  is unassailable. Comparison with the histogram of  $E_0$  values obtained from region II makes this very clear.

*Gap maps:* Figs. 5a and S4 were generated from the  $E_0(x, y)$  maps described above. The standard deviation of  $E_0$  over a box of size 3 pixels  $\times$  3 pixels, centered on each pixel, was collected over the extent of the image. The standard deviation was multiplied by  $2\sqrt{2}$  in order to obtain the local energy gap. This scaling is exact only for a perfectly bimodal distribution of  $E_0$  values. Fig. 3c (top) shows that histogram peaks A and B have finite widths. Because these widths also contribute to the

standard deviation, the energy gap  $\Delta = E_0(B) - E_0(A)$  is slightly overestimated [ $E_0(A)$  and  $E_0(B)$  denote energies of the respective histogram peaks]. The size of the calculation box and the influence of defect potentials creates some artifacts, but  $\Delta$  obtained from the rapid spatial variations is generally large by comparison.

*Data animation:* The data animation provided with this Supplementary Information is raw  $dI/dV$  map data, spline interpolated in energy to obtain a higher point (frame) density. This provides smoother transitions between frames without introducing artifacts in the spatial distribution because the  $LL_0$  peaks are well-defined at each pixel.

## II. SUPPLEMENTARY DATA

In this section we present further discussion and data demonstrating the spatially-periodic lifting of the valley degeneracy and addressing other issues.

*Filling factor:* The filling factor depends on the location of the Fermi energy within the  $LL^{av}$  spectrum. For all of the magnetic fields presented, the Fermi energy lies between the  $N = 0$  and  $N = -1$  levels, so the filling factor is constant at  $\nu = -2$ . The Fermi energy  $E_F$  occurs at zero sample bias in tunnelling spectra, well below  $LL_0^{av}$ , as is apparent from Fig. 2a (the  $N = -1$   $LL^{av}$  lies tens of meV below  $E_F$ ). At zero magnetic field  $LL_0^{av}$  lies  $\approx 6$  meV below  $E_F$ . As in prior work,<sup>1</sup> the energy of  $LL_0$  is found to depend on the magnetic field. This is discussed in Ref.1. The matter awaits a full theoretical calculation, however, the general explanation is that the field-dependent position of  $LL_0$  is a consequence of screening the electric fields from the substrate (which induces electron doping) and to some extent from the STM tip (which would tend to induce hole-doping due to the workfunction difference). The defect in the imaged area may also contribute to the charge density, partially pinning the Fermi level to an energy below  $LL_0^{av}$ .

*Valley splitting:* In Fig. S1 we show a second series of spectral profiles (compare Fig. 4) taken

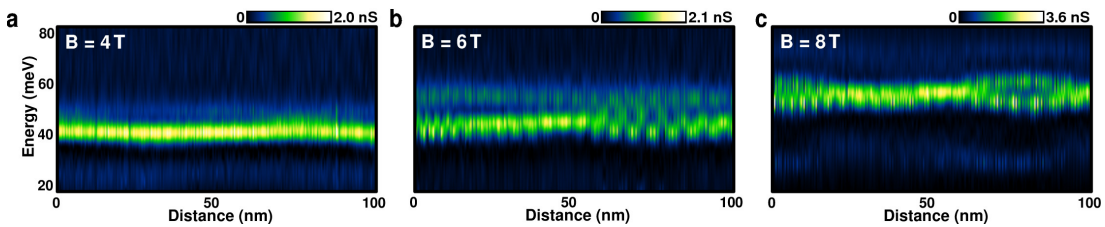


FIG. S1: Spectral profiles through the center of the map for magnetic fields of (a) 4 T, (b) 6 T, (c) 8 T.

along a horizontal line near the center of the Fig. 1a (the line passes through box I in Fig. 3a). From the nearly constant energy of  $LL_0$  in Fig. S1a it is apparent that the mean potential varies little in this region. Consequently, the energy gap appears symmetric in the 8 T spectral profile of Fig. S1c. The enhanced intensity of the high-energy satellite peak seen in Fig. S1b is still unexplained (see next subsection). As in Fig. 4, anticorrelation of intensity in the two bands is apparent. Aliasing is apparent in the bunching of bright/dark regions along the lines in each band. These bunches do not correlate with the short-period moiré, and their period can vary slightly [compare, e.g., the bunching in regions to the left (beginning) and right sides of the profiles].

The pixel-to-pixel variation of the  $LL_0$  peak intensity can be seen directly in the raw  $dI/dV$  maps by overlaying maps acquired near  $E_0(A)$  and  $E_0(B)$ . This is shown for 8 T maps in Fig. S2. Part (a) of the figure shows  $E_0^{av} - 4 \text{ meV} \approx E_0(A)$  in red and part (b) shows  $E_0^{av} + 4 \text{ meV} \approx E_0(B)$ . The two

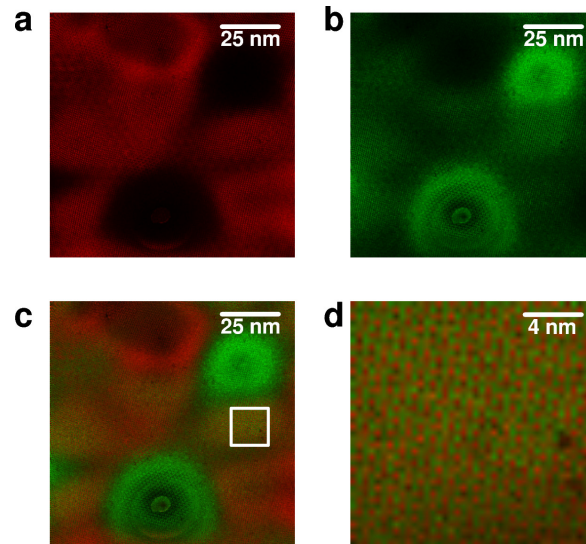


FIG. S2: Sublattice polarization seen in the raw  $dI/dV$  data acquired at a magnetic field of 8 T. Images were taken (a) at 52 meV,  $\approx 4 \text{ meV}$  below the  $LL_0^{av}$  peak (see Fig. 2a), and (b) at 60 meV,  $\approx 4 \text{ meV}$  above the  $LL_0^{av}$  peak. In (a)/(b), zero differential conductance is shown as black and the maximum differential conductance of 5 nS is red/green. (c) The sum of red and green images in (a) and (b). The speckled patch marked by a white box is shown expanded in (d).

maps are overlaid in Fig. S2c, and an expanded view of a speckled patch is shown in Fig. S2d. Color intensities are summed in the overlay images, producing yellow when the red and green intensities are equal. One can see distinct red and green pixels in the speckled region, consistent with sublattice polarization of the LDOS.

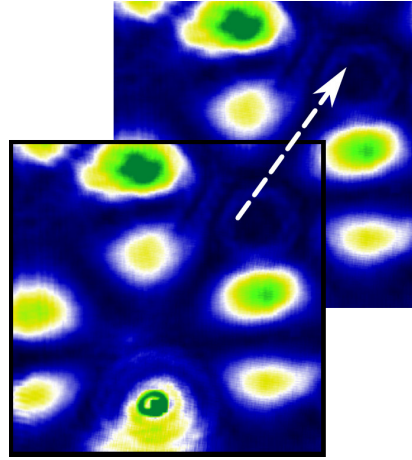


FIG. S3: The 8 T gap map of Fig. S4c (black outline) shown on top of the same map shifted in position by a moiré superlattice period (white arrow).

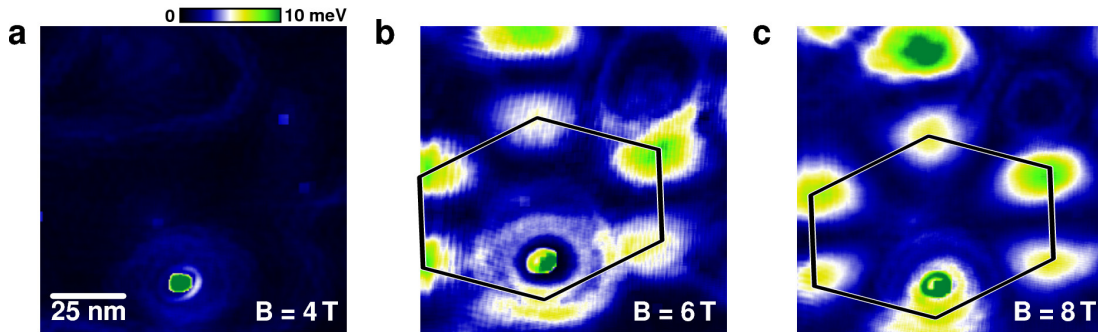


FIG. S4: Gap maps ( $\Delta(x, y)$ ) for magnetic fields of (a) 4 T, (b) 6 T, (c) 8 T. The quasi-hexagonal figures in (b) and (c) are identical. Note that maps at different magnetic fields are not in exact registry; the defect (bottom-center) can be used to judge positional displacement between maps.

Figure S3 demonstrates that the faint regions of increasing brightness seen at the upper-right edges of Fig. 5a [see also Figs. S4(b,c)] are consistent with an extended periodic moiré pattern. Similar shifts match with other edge-truncated patches in the map.

Figure S4(a,b,c) shows  $\Delta(x, y)$  gap maps at respectively, 4 T, 6 T, and 8 T (the 8 T gap map is identical to Fig. 5a, reproduced here for convenience). In Fig. S4a,  $\Delta$  remains close to zero, except near the defect at bottom-center. Over the defect the spectrum changes character, causing artifacts. The color scale should not be interpreted as the valley splitting  $\Delta$  within a radius of order  $\ell_B$  from the defect. A clear change in the spatial pattern is apparent in Fig. S4b, with distinct patches of large  $\Delta$ . This pattern is unchanged in Fig. S4c except for a slight increase in the magnitude of  $\Delta$  within the patches.

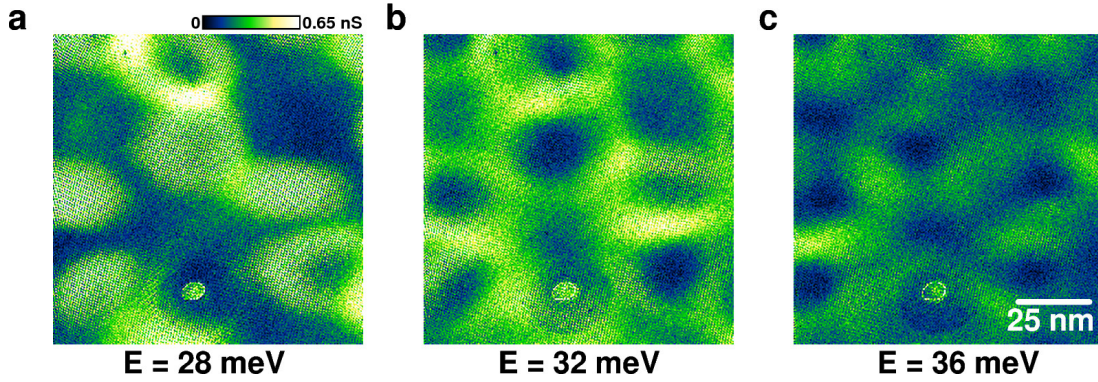


FIG. S5:  $dI/dV$  maps of the low-energy satellite peak taken at a magnetic field of 8 T. With respect to the spatially-averaged spectrum (Fig. 2a), the map energies progress from (a) just below the satellite peak, to (b) near the maximum of the satellite peak, to (c) just above the peak.

*Satellite Peaks:* The origin of the satellite peaks is not yet known. In Fig. S5 we show  $dI/dV$  maps for energies progressing over the low-energy satellite peak. Although the signal-to-noise ratio is smaller, the progression of spatial patterns is similar to that seen in Figs. 2(j,k,l) for the main  $LL_0^{av}$  peak. The same speckled patches can be seen, especially in Fig. S5a. Hence, the origin of this satellite seems to be related to the main  $LL_0^{av}$  peak. Equivalent data for the high-energy satellite is less revealing, perhaps because it lies in the tail of the main peak.

Tentatively excluding interaction effects for reasons mentioned in the main text, there are still several possibilities for the origin of these satellites. For example, they could be due to coherent coupling to lower layers,<sup>2</sup> they may be defect-related,<sup>3</sup> Coulomb-charging may play a role (due to weak coupling of a tip-induced quantum dot to its surroundings), and inelastic events can't yet be excluded. Coupling of wavefunctions from different AB/BA patches may also contribute. A resolution of these issues requires further experiments.

### III. THEORY

Here we outline the phenomenological model of sublattice symmetry breaking suggested in the main text as a possible explanation of our findings. With the motivation given in the main text we assume that the observed sublattice polarization is due to the coupling of the top graphene layer to the third layer counted from the top. In the intuitive picture presented in the main text, this interlayer coupling creates a staggered potential  $V_{AB}$  that differs in sign between the A and the B sublattices

and thus breaks the sublattice symmetry. Since the interlayer registry varies spatially within the corresponding moiré pattern,  $V_{AB}$  varies on a hexagonal superlattice associated with the interlayer rotation. In our experiment the period of that superlattice is  $\ell \approx 70$  nm (the spacing between AB and BA patches is  $\approx 40$  nm). In a first, minimalistic analysis of our model, presented below, we attempt to capture only the essential physics needed to understand the experimental data. For this reason we disregard the space dependence of  $V_{AB}$  in the direction perpendicular to the lines along which the spectra of Fig. 4 were taken:  $V_{AB} = \bar{V}_{AB} \cos 2\pi x/\ell$ .

The low-energy Hamiltonian of graphene, the so-called Dirac Hamiltonian, reads

$$H_\gamma = v_F \boldsymbol{\sigma}_\gamma \cdot \left( \frac{\hbar}{i} \boldsymbol{\nabla} - e \mathbf{A}(\mathbf{r}) \right) + m(\mathbf{r}) v_F^2 \sigma_z + V(\mathbf{r}), \quad (1)$$

where  $\boldsymbol{\sigma}_\gamma = (\sigma_x, \gamma \sigma_y)$  is a vector of Pauli matrices,  $\gamma = \pm$  an orbital degree of freedom called valley spin,  $-e$  the electron charge, and  $v_F$  the electron velocity in graphene. We have included a scalar and a vector potential  $V$  and  $\mathbf{A}$ , respectively, and a mass  $m$  for the Dirac electrons. The Hamiltonian  $H_\gamma$  acts on two-component spinor wavefunctions, containing the separate amplitudes for an electron to be on the A- and the B-sublattice, respectively. A staggered potential with  $V_{AB} > 0$  has a positive value on the A-sublattice and a negative value on the B-sublattice. In the above low-energy spinor description,  $V_{AB}$  is thus accounted for by a term  $\propto \sigma_z$ . We therefore describe the top layer of the measured samples by  $H_\gamma$ , Eq. (1), with  $\mathbf{A}(\mathbf{r}) = (0, Bx)$ ,  $V(\mathbf{r}) = 0$ , and a mass term  $m(\mathbf{r}) v_F^2 = \bar{V}_{AB} \cos 2\pi x/\ell$ . We extract  $\bar{V}_{AB}$  phenomenologically from the magnitude of the observed splitting of  $\text{LL}_0$  by means of Eq. (2). In our experiment we have  $\bar{V}_{AB} \ell / \hbar v_F \ll 1$  and thus we solve the corresponding Schrödinger equation perturbatively, to first order in the parameter  $\chi = \min\{\ell, \ell_B\} \times \bar{V}_{AB} / \hbar v_F$ . To that accuracy we find the eigenenergies

$$\varepsilon_\gamma = \gamma \bar{V}_{AB} e^{-\pi^2 \ell_B^2 / \ell^2} \cos \frac{2\pi x_0}{\ell} \quad (2)$$

of the wavefunctions in  $\text{LL}_0$  that are centered around  $x = x_0$ . We observe that  $\text{LL}_0$  indeed consists of two bands of wavefunctions with a spatially modulated energy splitting between each other, as observed experimentally (see Figs. 3, 4, and S1). The corresponding wavefunctions are distinguished by the valley degree of freedom  $\gamma$ . The total electron density in  $\text{LL}_0$  with  $\gamma = 1$  (i.e., the density of states integrated over energies within the peak of  $\text{LL}_0$  at  $\gamma = 1$  in case that peak is clearly split from  $\text{LL}_0$  at  $\gamma = -1$ ) is found to be  $\rho_A = (1/\pi \ell_B^2)[1 + \mathcal{O}(\chi)^2]$  on the A sublattice and  $\rho_B = \mathcal{O}(\chi)^2 \ll \rho_A$  on the B sublattice, confirming the sublattice polarization of the two branches of  $\text{LL}_0$  assumed in the main text. The densities found for  $\text{LL}_0$  in the  $\gamma = -1$  valley are identical to the above, but the roles

of the A and the B sublattices are interchanged. The above model thus reproduces three of the main qualitative features of the spectra shown in Fig. 4:

- There is an oscillatory splitting of the zeroth Landau level into two bands of wavefunctions with energies  $\pm \bar{V}_{AB} \cos \frac{2\pi x_0}{\ell}$  at  $\ell \gg \ell_B$ .
- The wavefunctions in each of the split bands separately are sublattice-polarized. This implies an anticorrelation between the densities of states in those two bands on the lattice scale, also indicated by the STS measurement.
- There is an exponential suppression of the level splitting at weak magnetic fields by the factor  $\exp(-\pi^2 \ell_B^2 / \ell^2)$ . Also such a suppression at small magnetic field is clearly observed experimentally (note that the experimental energy resolution in Fig. 4 is 4 meV, such that the observed absence of a gap at  $B = 4$  T is entirely consistent with the above theory if the predicted suppression of the gap is sufficiently strong.).

The effects of the smaller moiré pattern observed in STM topography with  $\tilde{\ell} \approx 4$  nm (most likely due to interaction with the second graphene layer from the top) can be analyzed similarly. One finds that it has a negligible effect because  $\tilde{\ell} \ll \ell_B$ .

The above phenomenological model can be placed on a microscopic foundation by integrating out the third graphene layer in a tight-binding model of the sample, arriving at an effective Hamiltonian  $H_{\text{eff}}$  of the top layer. In such a derivation the postulated staggered potential  $V_{AB}$  results from the local (in space) and energy-independent contributions to  $H_{\text{eff}}$ . Strictly speaking, neither the energy-dependence nor the non-local contributions to  $H_{\text{eff}}$  can be neglected (the non-locality increases with decreasing magnetic field, such that the above intuition invoking a staggered potential is in general not useful for a bilayer in zero field). Nevertheless, a careful analysis (to be presented elsewhere) shows that the conclusions drawn from the simplified, local model presented above are qualitatively correct. The magnitude of the staggered potential obtained by integrating out the third graphene layer is readily estimated in perturbation theory, when the on-site energies of atoms receive (sublattice-dependent) corrections of order  $|\gamma_5|^2 / \Delta\varepsilon$ . Here,  $\gamma_5 \approx 25$  meV<sup>4,5</sup> is the next-nearest layer hopping amplitude. The scale of the energy denominator  $\Delta\varepsilon$  is set by the difference  $\Delta V$  between the chemical potentials of layer 1 and layer 3 (the energy  $\approx 50$  meV needed to tunnel into LL<sub>0</sub> of the top layer suggests  $\Delta V \approx \gamma_5$ ), and the cyclotron energy. The value of  $\bar{V}_{AB}$  extracted above phenomenologically

is thus of the microscopically expected order of magnitude  $\bar{V}_{AB} \approx |\gamma_5|^2/\Delta\epsilon$ .

---

\* first@gatech.edu

† joseph.stroschio@nist.gov

- <sup>1</sup> Miller, D. L. *et al.* Observing the quantization of zero mass carriers in graphene. *Science* **324**, 924–927 (2009).
- <sup>2</sup> Mele, E. J. Commensuration and interlayer coherence in twisted bilayer graphene. *Phys. Rev. B* **81**, 161405(R) (2010).
- <sup>3</sup> Pereira, A. L. C. & Schulz, P. A. Additional levels between Landau bands due to vacancies in graphene: Towards defect engineering. *Phys. Rev. B* **78**, 125402 (2008).
- <sup>4</sup> Dresselhaus, M. S. & Dresselhaus, G. Intercalation compounds of graphite. *Adv. Phys.* **51**, 1–186 (2002).
- <sup>5</sup> Partoens, B. & Peeters, F. M. From graphene to graphite: Electronic structure around the K point. *Phys. Rev. B* **74**, 075404 (2006).